Research Article

Sonophotopythochemical Functionalization of Graphene Oxide - Al - Zn Bimetal Nanocomposite for Corrosion Inhibition

Carlou Siga-an Eguico, Maribel Mago Abanto, Hershey Tambo Cendaña, Denisse Anne Perez Famero, Kauthar Belandres Pediongco, Albert Dela Cruz Evangelista and Rugi Vicente Del Castillo Rubi*
Chemical Engineering Department, College of Engineering, Adamson University 900 San Marcelino St. Ermita, Manila, Philippines

* Corresponding author. E-mail: rugi.vicente.rubi@adamson.edu.ph

DOI: 10.14416/j.asep.2024.10.004
Received: 26 July 2024; Revised: 14 September 2024; Accepted: 27 September 2024; Published online: 9 October 2024

Abstract

The corrosion performance of steel in the marine environment has been a primary concern of engineers and garnered significant interest due to its industrial significance. To address this concern, the incorporation of green corrosion inhibitors as coating materials in mild steel has been extensively studied recently. This paper explores the synthesis of graphene doped with bimetal aluminum-zinc (GO-Al-Zn) nanocomposites via sonophoto-phytochemical functionalization using Chayote (*Sechium edule*) leaf extract as the doping agent to produce a corrosion inhibitor. The synthesized nanocomposites were characterized using FTIR, SEM-EDS, XRD, and TEM. The optimal nanocomposite, with a 55% Al - 45% Zn ratio, demonstrated successful bio-reduction, good dispersion, reduced particle size, and a rhombohedral crystal structure. When incorporated into an epoxy coating and applied to mild steel, the GO - 55% Al - 45% Zn coating achieved a high corrosion inhibition efficiency of 98.06% (gravimetric method) and 98.45% (electrochemical method) in 3.5 wt% NaCl solution. This study highlights the promising potential of GO - 55% Al - 45% Zn nanocomposite as an eco-friendly corrosion inhibitor. Future research should explore optimizing the functionalization process and exploring long-term environmental stability.

Keywords: Al-Zn Bimetallic, Corrosion inhibition, Graphene Oxide, Nanocomposite, Ultrasound, UV Radiation

1 Introduction

Mild steel is widely used in various industries, particularly in maritime applications such as pipeline systems, offshore oil infrastructure, and ship decks, due to its favorable mechanical properties, including toughness, ductility, and high yield strength [1]. However, despite these advantages, its susceptibility to corrosion in saltwater environments poses a significant threat to the structural integrity and economic viability of marine structures. Corrosion is influenced by factors such as temperature, pH, salinity, humidity, dissolved oxygen, and ultraviolet rays [2]. This issue necessitates the development of advanced corrosion protection technologies, as the degradation of metals can result in costly repairs and potential safety hazards in marine transportation [3].

Various anti-corrosion technologies, such as polymeric coatings, epoxy coatings, and anti-corrosion paints, have been developed and widely studied across different countries. These coatings offer benefits such as flexibility, processability, chemical resistance, and thermal stability [4]. However, environmental concerns and economic limitations associated with existing technologies have spurred the search for more sustainable solutions [5]. Recent advancements in nanocomposites have shown promising potential to surpass the performance of conventional coatings, particularly in terms of corrosion resistance [6]. Nanocomposites, especially those incorporating Graphene Oxide (GO), have attracted significant interest due to GO's excellent dispersion properties, which enhance the overall performance of anti-corrosion coatings. The synergistic interaction between GO and metals like aluminum and zinc nanoparticles further boosts corrosion resistance, making these nanocomposites more effective than single-material coatings [7], [8].

This study focuses on the synthesis of a novel GO-Al-Zn bimetallic nanocomposite using a green approach, incorporating Chayote (*Sechium edule*) leaf extract for bio-reduction and stabilization. Chayote extract, rich in flavonoids and phenols, has been shown to enhance nanoparticle stabilization and reduction [9]. The use of eco-friendly phytochemical functionalization offers a non-toxic alternative to traditional coating additives [10], [11]. Furthermore, combining sonication and UV radiation, referred to as the sonophoto-phytochemical method, resolves common challenges in nanoparticle synthesis by improving particle dispersion, size reduction, and stabilization [12]. This study aims to explore the morphology, composition, and corrosion inhibition potential of the GO-Al-Zn nanocomposite in a marine environment, contributing to the development of environmentally friendly anti-corrosion technologies.

2 Methods

2.1 *Preparation of Chayote (Sechium edule) leaves*

Chayote (*Sechium edule*) leaves were sourced from Baguio City, Philippines, and taxonomically identified by the Bureau of Plant Industry. The leaves were washed thoroughly with running water, followed by deionized water to remove contaminants. They were then air-dried for three days in a well-ventilated room until crisp. The dried leaves were pulverized using a mechanical grinder, passing through Mesh 200 to obtain a fine powder, which was stored in sealed containers at room temperature.

Fifty grams of the powdered leaves were weighed and then mixed with water in a 1:4 solute-to-solvent ratio in an Erlenmeyer flask. This suspension was placed in a rotary shaker bath for maceration at 60 °C for 2 h. After cooling, the extract was filtered twice—first for larger impurities and then for smaller particles. The filtered extract was stored in an amber bottle at 4 °C until further use.

2.2 *Synthesis of GO-Al-Zn nanocomposite*

Three mixtures of GO-Al-Zn nanocomposite were prepared with varying Al-Zn ratios: 1) 5% Al - 95% Zn + GO, 2) 15% Al - 85% Zn + GO, and 3) 55% Al - 45% Zn + GO. Each mixture underwent synthesis treatments: sonication, UV radiation, and a combination of both at different time exposures (10, 15, and 20 min). After treatment, the mixtures were centrifuged at 10,000 rpm for 15 min to separate precipitated particles, which were then filtered and washed multiple times. The cleaned precipitates were dried in a convection oven at 40 °C, followed by calcination at 500 °C for 3 h. The calcined material was crushed and passed through US Mesh #450, and the final nanocomposites were stored in sealed containers.

Rectangular steel coupons were prepared following ASTM standards for strip coupons. Each steel coupon measured 1.0 × 2.0 × 0.118 inches, with a geometric area variation maintained within ±1% to ensure consistency. The top surface of each coupon underwent oxide layer removal using a sequence of emery papers with varying grit sizes: 120, 150, and 200 grit. The coupons were rinsed with deionized water on multiple occasions to eliminate any residual particles from the abrasion step. The coupons were subsequently submerged in denatured alcohol within a sonicator bath. Finally, the cleaned coupons were stored in a desiccator until their designated use to minimize contamination and maintain a controlled environment.

2.3 *Preparation of steel coupons and coating*

Rectangular steel coupons (1.0 × 2.0 × 0.118 inches) were prepared according to ASTM standards. The oxide layer was removed using emery papers (120, 150, and 200 grit), followed by thorough rinsing with deionized water. The coupons were then sonicated in denatured alcohol and stored in a desiccator.

The nanocomposite with the highest yield from the synthesis treatments was dispersed into an epoxy resin matrix, prepared in a 2:1 ratio of parts A and B. Nanocomposite loadings of 0.5 wt%, 1.0 wt%, and 1.5 wt% were incorporated into the resin, along with 5 wt% denatured alcohol to ensure uniform dispersion. The mixture was sonicated and then applied onto the steel coupons using an air gun sprayer, with 2–3 coats applied and air-drying for 1 h between coats. The coated coupons were cured in a convection oven at 40 °C for 6 h, and then allowed to cool before characterization and testing.

2.4 *Weight Loss Method and Characterization*

To simulate seawater environment, a 3.5 wt% NaCl solution was prepared. This involved dissolving 35 grams of NaCl in 1 L of deionized water within a non-reactive container. The prepared coated steel coupons were carefully placed inside the container and labeled for proper identification. The container was filled with the prepared NaCl solution and ensure complete submersion of all samples.

The simulation was designed to mimic a seawater condition, the container was maintained at ambient pressure and a controlled temperature range of 20 °C to 45 °C. To minimize solution volume fluctuations, the level was monitored and maintained within ±1% of the initial volume. A closed container system was employed to prevent any potential evaporation losses.

Following the designated exposure durations (7 days, 14 days, and 21 days), the samples were retrieved from the simulated seawater environment. A meticulous examination was conducted to assess any signs of corrosion attack, pitting, or other relevant observations pertinent to the study. To evaluate the extent of potential degradation, a mechanical cleaning process was implemented, involving scraping and scrubbing to remove any anti-corrosion materials that may have adhered to the sample surfaces. Subsequently, the samples were thoroughly rinsed with deionized water on multiple occasions to remove any residual contaminants introduced during the immersion. After rinsing, the samples were degreased using denatured alcohol and allowed to air-dry completely. Finally, the cleaned samples were stored within a desiccator for 24 h to ensure complete desiccation. Following this drying period, the final weight of each sample was measured again using an analytical balance to quantify any potential mass changes due to the simulated seawater exposure.

The weight loss and their differences can be used to calculate inhibition efficiency (η%) and corrosion rate (Cr) by following Equations (1):

$$\eta\% = \frac{W_o - W_i}{W_o} \times 100 \tag{1}$$

Where W_o is the weight loss when an inhibitor is not present, W_i is the weight loss when an inhibitor is present.

The corrosion rate (CR) is calculated in mils penetration per year (mpy) from the following Equation (2):

$$CR\ (mpy) = \frac{KW}{AtD} \tag{2}$$

where K is a constant 3.45×10^6 data, W is the weight loss in grams, A is the specimen area in cm², t is a time of exposure in hours and d is the density of carbon steel at 7.86 g/cm³.

2.5 *Tafel plot*

Tafel data acquisition was achieved using a scanning potentiostat in a three-electrode cell configuration. The working electrode was comprised of the mild steel substrate, while a stainless steel electrode served as the counter electrode, and an Ag/AgCl electrode functioned as the reference electrode. To mimic the simulated seawater environment, a 150 mL reference test solution containing 3.5 wt% NaCl was prepared using deionized water.

All electrochemical measurements were conducted at room temperature using a Metrohm Autolab PGSTAT128N potentiostat/galvanostat within the three-electrode setup. The exposed working electrode area within the electrolyte solution was maintained at a constant 1 cm^2. Prior to commencing the actual measurements, meticulous calibration of the testing materials and verification of the apparatus functionality, including proper data acquisition, were performed.

Linear sweep voltammetry (LSV) was employed to obtain the Tafel data. The LSV measurements utilized a line sweep rate of 1.25 mV/s across a potential range of ± 250 mV. The resulting data was then plotted as a linear polarization curve, depicting the relationship between potential and current density. The polarization resistance (Rp) was subsequently determined by analyzing the tangent of the curve at the point where the current density i = 0.

The polarization resistance Rp in ohm-cm^2 is calculated using the following Equation (3):

$$R_p = \frac{b_a b_c}{2.303(b_a + b_c) i_{corr}} \tag{3}$$

Where b_a is the anodic Tafel slope, b_c is the cathodic Tafel slope, and i_{corr} corrosion current density.

To compute the corrosion rate (CR) in mm per year, it was calculated using the following Equation (4):

$$CR = 3.27 \times 10^{-3} \frac{i_{corr} EW}{\rho} \tag{4}$$

Where i_{corr} is the corrosion current density in µA/cm^2, *EW* is the equivalent weight of the corroding species in grams and is the density of the corroding material in g/cm^3.

3 Results and Discussions

3.1 *Characterization of GO-Al-Zn bimetal nanocomposite from different treatments*

3.1.1 Fourier Transform Infrared Spectroscopy (FTIR) of GO-Al-Zn nanocomposites

The FTIR spectra presented in Figure 1 and Table 1 provide detailed information on the functional groups identified in the GO-Al-Zn bimetal nanocomposite. These results revealed important insights into the structural composition of the material synthesized using different methods. The analysis confirms the presence of various functional groups consistent with findings from the literature [13]–[15], particularly related to the components of graphene oxide (GO), aluminium (Al), and zinc (Zn). This detailed examination of the nanocomposite's chemical makeup is essential for understanding its potential applications, particularly in the area of corrosion inhibition.

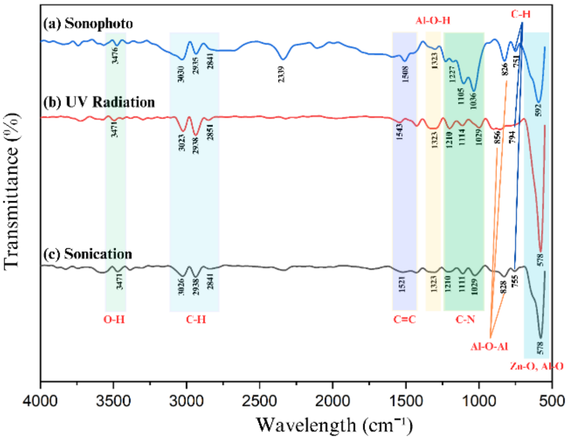

Figure 1: FTIR analysis of (a) sonophoto, (b) UV radiation, and (c) sonication treatments on GO-Al-Zn bimetal nanocomposites.

Table 1: Functional groups of Fourier Transform Infrared (FTIR) spectroscopy for GO-Al-Zn nanocomposites.

Functional Groups	Sonophoto		UV Radiation		Sonication	
	Wavenumber (cm^{-1})	Intensity	Wavenumber (cm^{-1})	Intensity	Wavenumber (cm^{-1})	Intensity
O-H	3476	Weak	3471	Weak	3471	Weak
C-H stretch	3030	Weak	3023	Weak	3026	Weak
C-H bend	2935	Weak	2938	Medium	2938	Weak
C-H stretch	2841	Weak	2851	Weak	2841	Weak
CO_2 bend	2339	Medium	2322	Weak	2333	Weak
C=C	1508	Weak	1543	Weak	1521	Weak
Al-O-H bend	1323,1301	Medium	1323	Medium	1323	Weak
C-N (primary amine)	1227	Weak	1210	Medium	1210	Weak
C-N (secondary amine)	1105, 1036	Strong	1114,1029	Weak	1111,1029	Weak
Al-O-Al	826	Medium	956	Weak	828	Weak
C-H	751	Medium	794	Weak	755	Weak
Zn-O Al-O	592	Medium	578	Strong	578	Medium

In the single bond region (2500–4000 cm^{-1}), prominent peaks corresponding to O−H bonds were observed at 3476, 3471, and 3471 cm^{-1}, indicating the presence of hydroxyl groups. These O−H bonds are primarily associated with GO, which is integrated into the composite alongside Al and Zn nanoparticles. Hydroxyl groups are known to contribute to the hydrophilic properties of the material, enhancing its dispersion within a matrix [16]. Additionally, C−H bonds were observed at 3030, 3023, 3026, 2841, 2851, and 2841 cm^{-1}, while C−H bends were detected at 2935, 2938, and 2938 cm^{-1}, confirming the presence of organic components from GO [16]. The C−H bond peaks, specifically in the 3000–2900 cm^{-1} range, suggest the existence of alkyl groups, which likely stem from the carbonaceous nature of GO. The repetition of these bonds across the different synthesis methods reinforces the assumption that GO successfully integrates into the bimetallic structure and remains chemically active after calcination [17].

In the triple bond region (2000–2500 cm^{-1}), a weak peak at 2339, 2322, and 2333 cm^{-1} indicates the presence of CO_2, which is consistent with previous studies that show CO_2 peaks appearing around 2300 cm^{-1} in FTIR spectra [17]. This CO_2 may be a by-product of the high-heat calcination process used during sample preparation. Although the presence of CO_2 is generally rare in uncalibrated FTIR instruments, its detection here highlights the importance of understanding thermal decomposition during the synthesis process, even when it does not directly impact the nanocomposite’s primary function.

The double bond region (1500–2000 cm^{-1}) revealed peaks at 1508, 1543, and 1521 cm^{-1}, corresponding to the C=C stretch. These findings are indicative of aromatic compounds, particularly those from graphene sheets, where unsaturated carbon bonds are typically present. The detection of C=C bonds suggests that the graphene structure within the composite remains intact after synthesis, preserving its mechanical strength and electrical conductivity—properties essential for various advanced applications [14].

The fingerprint region (500–1500 cm^{-1}) provided the most distinctive information about the nanocomposite’s composition. Peaks at 1323 and 1301 cm^{-1} correspond to Al−O−H bonds, while peaks at 826, 856, and 828 cm^{-1} suggest Al−O−Al bonding, confirming the successful incorporation of aluminium nanoparticles into the composite. Additionally, Zn–O bonds were observed at 751, 755, and 794 cm^{-1}, indicating the presence of zinc nanoparticles. These findings confirm the bimetallic nature of the nanocomposite, proving that both Al and Zn have been successfully integrated with graphene oxide during the synthesis process [18].

Furthermore, weak peaks at 1227 and 1210 cm^{-1} revealed the presence of primary amine C−N groups, while secondary amine C−N groups were detected at 1105, 1036, 1029, 1111, and 1029 cm^{-1}. These nitrogen-containing functional groups likely result from the use of natural extracts (such as chayote), which contribute to the formation of the nanocomposite structure. The presence of both oxygen and nitrogen atoms in these functional groups plays a crucial role in the effectiveness of the nanocomposite for corrosion inhibition, as these atoms help form stable protective layers on metal surfaces [18].

The presence of various functional groups, including O−H, C−H, C=C, and C−N, indicates that the nanocomposite has a complex yet well-integrated structure. The oxygen-containing groups, particularly hydroxyl and carbonyl functionalities, enhance the material’s anticorrosion properties by interacting with metal surfaces and forming a protective layer that inhibits oxidation [19]. Additionally, nitrogen-containing groups from amines contribute to corrosion resistance by creating stable complexes with metal ions. Together, these functional groups make the nanocomposite chemically robust and suitable for protective coatings in harsh environments [14], [18].

The detection of aluminium and zinc, as confirmed by the FTIR analysis, underscores their role in enhancing the material's mechanical and anticorrosion properties. Both Al and Zn are known for their ability to form passive oxide layers, which provide excellent resistance to corrosion. The presence of Al−O and Zn−O bonds reinforces the protective characteristics of the nanocomposite, making it ideal for applications in environments that demand strong anticorrosion performance [15], [19].

Additionally, the natural extracts from chayote, rich in flavonoids and phenolic compounds, likely influence the functional properties of the nanocomposite. These phytochemicals are known to exhibit antioxidant activity, which could further enhance the material’s corrosion-inhibiting abilities by scavenging free radicals and preventing oxidative damage to the metal surface [20]. This highlights the synergistic interaction between the natural extracts and the bimetallic components, contributing to the overall performance of the nanocomposite.

The FTIR analysis provides strong evidence of the successful synthesis of the GO-Al-Zn bimetal nanocomposite. The identified functional groups contribute significantly to the material's stability, corrosion resistance, and potential for use in protective coatings. The presence of oxygen- and nitrogen-containing groups, along with the incorporation of aluminium and zinc nanoparticles, suggests that this nanocomposite is chemically robust and well-suited for advanced applications [10], [19]. Future research could focus on optimizing the synthesis process to further enhance the dispersion and interaction of these functional groups, potentially improving the material's performance in real-world applications.

3.1.2 SEM results of GO-Al-Zn bimetals nanocomposite

The Scanning Electron Microscopy (SEM) images presented in Figure 2 provide a detailed visualization of the morphology and structure of the GO-Al-Zn bimetal nanocomposite (NCs) produced through different synthesis methods. The images revealed significant differences in particle shapes and sizes across the various treatments, demonstrating how synthesis methods affect the nanocomposite’s physical properties.

Figure 2(a) GO-Al-Zn nanocomposite synthesized via ultrasonic-assisted processes exhibits irregular particle shapes and a broad size distribution. Ultrasonication, which induces cavitation, is primarily responsible for this morphology. Cavitation involves the rapid formation, growth, and collapse of bubbles in the liquid medium, which generates localized high-pressure and high-temperature zones [19]. These intense conditions result in the formation of nanoparticles, albeit with irregular surface structures due to the dynamic nature of the cavitation process. This irregularity in shape and size indicates a degree of inconsistency in particle formation, which is typical for processes driven by mechanical energy alone [14]. While the cavitation effect aids in the distribution of nanoparticles, it may also cause uneven stress and energy dissipation across the medium, leading to the formation of particles with varied geometries.

On the other hand, Figure 2 (b) synthesized using UV radiation revealed agglomerated particles with smoother, but still irregular, surfaces. The agglomeration observed in the UV-assisted process is likely due to the formation of additional nucleation centers during exposure to UV light [20]. UV radiation stimulates the creation of free radicals and active sites on the GO surface, which enhances the bonding between the bimetal nanoparticles and the GO sheets. However, the downside of this process is the tendency for nanoparticles to clump together, as these active sites encourage agglomeration, leading to larger clusters of particles [20]. Despite this, the average particle size is smaller compared to the sonication process. UV radiation induces the breakdown of the polymer matrix within graphene, facilitating the reduction in particle size by creating finer nanoparticles through polymer fragmentation [21]. This particle size reduction is a critical factor in enhancing the surface area of the nanocomposite, which directly impacts its functional properties, such as corrosion resistance.

Lastly, Figure 2(c) synthesized through the sonophoto method (a combination of sonication and UV radiation) exhibits a highly agglomerated yet finer distribution of nanoparticles. The bulk amorphous surface observed suggests that the synergy between sonication and UV radiation refines the morphology and enhances the dispersion of smaller nanoparticles [20]. The sonophoto method effectively combines the advantages of both sonication and UV radiation: sonication helps reduce particle size, while UV radiation further narrows the size distribution and fine-tunes the surface structure of the nanoparticles [20], [22]. The resulting nanoparticles are more homogenous in terms of size and structure, which can be attributed to the dual impact of cavitation and UV-induced nucleation. This method’s enhanced control over particle morphology and size distribution has been shown to improve the material's overall performance, particularly in applications requiring high surface area and uniform nanoparticle coverage [20].

The differences in particle size and morphology across the various synthesis methods highlight the importance of process selection in nanocomposite production. The irregular shapes produced by sonication could hinder the homogeneity required for certain applications, despite its ability to create a broader particle size distribution. On the other hand, UV radiation demonstrates better control over particle size but at the cost of increased agglomeration, which could reduce the available surface area of the nanocomposite.

The sonophoto method presents the most promising results, achieving a balance between particle size reduction and improved particle dispersion. However, the tendency toward agglomeration, even in this optimized method, suggests that additional post-synthesis treatments, such as surface modification or the use of dispersing agents, may be necessary to further improve the material's properties [19], [22].

Each synthesis method exhibits unique advantages and drawbacks. The sonophoto method outperforms the others by offering a better balance between size reduction and uniform particle distribution, although further optimization is required to minimize agglomeration. Future research should focus on refining the sonophoto method and exploring the long-term stability of these nanocomposites in practical applications.

3.1.3 EDS analysis of the GO-Al-Zn bimetal nanocomposite

Figure 3 shows the Energy Dispersive Spectroscopy (EDS) analysis of the GO-Al-Zn bimetal nanocomposite synthesized using different treatments: a) sonication, b) UV radiation, and c) sonophoto (combined sonication and UV radiation). The elemental compositions vary across the different treatments, shedding light on the effects of each method on nanoparticle synthesis and distribution.

In Figure 3(a), the EDS results for the sonication treatment revealed a composition of 43.0% oxygen, 19.1% aluminum, 16.2% zinc, and 15.3% carbon. This indicates that sonication successfully disperses Al and Zn nanoparticles within the GO matrix. Sonication creates cavitation effects—microscopic bubbles in the solution that expand and collapse, causing localized high temperatures and pressures. This cavitation facilitates the uniform distribution of nanoparticles on the graphene sheets, ensuring that Al and Zn are well-dispersed across the GO surface [18]. The relatively high oxygen content is attributed to the oxidation of GO during calcination and the inherent oxygen present in graphene oxide itself. This oxidation process is crucial as it enhances the stability and bonding of the metal particles to the graphene matrix.

In contrast, the EDS results for UV radiation treatment, shown in Figure 3(b), revealed a different composition: 39.0% oxygen, 24.6% carbon, 16.6% aluminum, and 14.2% zinc. The increase in carbon content and the decrease in oxygen compared to the sonication method suggest a significant breakdown of the GO polymer matrix under UV radiation. UV radiation can induce photo-degradation, leading to the breakdown of the carbonyl and carboxyl groups within the GO structure. This process not only creates more free carbon but also lowers the overall oxygen content by breaking oxygenated functional groups. This shift suggests that UV radiation may improve the structural integrity of the GO-Al-Zn nanocomposite by increasing carbon content while maintaining good metal distribution.

The EDS results for the sonophoto method in Figure 3(c) demonstrate 40.4% oxygen, 23.4% carbon, 16.1% zinc, and 13.2% aluminum. The composition here indicates a balanced effect of both sonication and UV radiation. The sonophoto method appears to leverage the strengths of both techniques: sonication ensures good particle dispersion, while UV radiation reduces the size of the nanoparticles. This synergistic effect results in smaller, well-distributed nanoparticles on the graphene matrix, as sonication provides cavitation and agitation, while UV radiation facilitates the breakdown of GO, reducing particle size and promoting more uniform nanoparticle deposition [20]. The stable nucleation and growth of nanoparticles are supported by the protective role of phytochemicals, such as flavonoids and phenols, present in the Chayote leaf extract. These phytochemicals act as capping agents, preventing agglomeration and enhancing nanoparticle stability [15].

Overall, the sonophoto treatment stands out as the most effective method, combining the advantages of sonication and UV radiation to achieve a better balance between particle size reduction and distribution. The increased stability of the nanoparticles can be attributed to the bio-reduction capability of the phytochemicals, which not only stabilize the nanoparticles but also enhance the anti-corrosion properties of the final nanocomposite product. This result is consistent with previous studies on hybridized nanocomposites, which emphasize the importance of particle size and distribution in determining the effectiveness of nanomaterials for industrial applications, including corrosion inhibition [19].

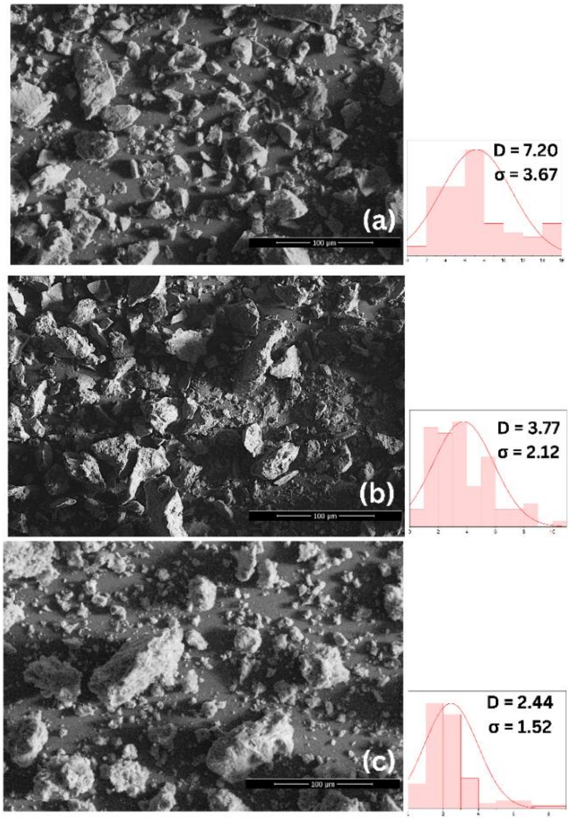

Figure 2: SEM Results of GO-Al-Zn Bimetals Nanocomposite by (a) Sonication, (b) UV Radiation, (c) Sonophoto.

The EDS analysis confirms that the sonophoto method is the most promising for achieving optimal nanoparticle characteristics. The improved dispersion and reduced particle size are key factors for enhancing the surface area of the nanocomposite, which directly contributes to its improved performance in applications like corrosion inhibition. However, a limitation of this study is the focus on specific synthesis parameters, such as time and temperature, without exploring a broader range of conditions. Future research should investigate the effects of varying these parameters to further optimize the synthesis process. Additionally, long-term stability tests are needed to assess the durability of the nanocomposite under real-world conditions, particularly in marine environments, where factors like temperature fluctuations and prolonged UV exposure may affect the material's performance.

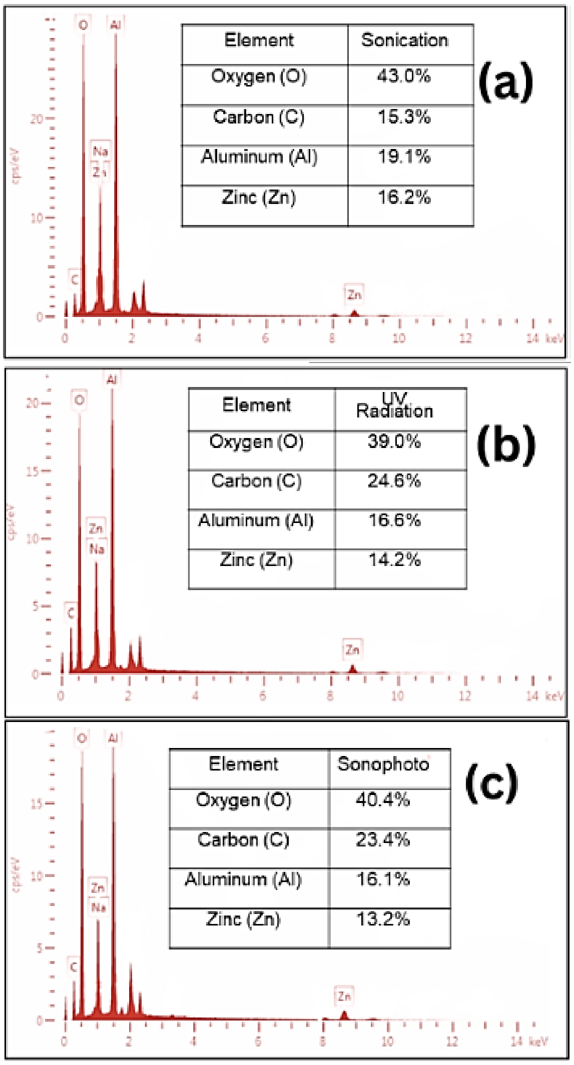

Element	Sonication
Oxygen (O)	43.0%
Carbon (C)	15.3%
Aluminum (Al)	19.1%
Zinc (Zn)	16.2%

Element	UV Radiation
Oxygen (O)	39.0%
Carbon (C)	24.6%
Aluminum (Al)	16.6%
Zinc (Zn)	14.2%

Element	Sonophoto
Oxygen (O)	40.4%
Carbon (C)	23.4%
Aluminum (Al)	16.1%
Zinc (Zn)	13.2%

Figure 3: EDS Analysis of the GO-Al-Zn Bimetal Nanocomposite by (a) Sonication, (b) UV Radiation, and (c) Sonophoto.

3.1.4 XRD results of GO-Al-Zn bimetals nanocomposite

The XRD analysis is a critical tool for predicting the plane geometry of crystal structures and determining the crystalline size of particles within nanocomposites. Sharp and prominent peaks in the XRD patterns indicate high crystallinity and a lack of impurities in the nanoparticles, which are essential characteristics for applications requiring stable and consistent nanomaterials. In the case of the GO-Al-Zn bimetal nanocomposite, the XRD patterns in Figure 4 revealed significant information about its crystalline structure and size, which differ based on the synthesis method used.

For the sonication treatment Figure 4(c), the XRD peaks occur at approximately 23°, 26°, 33°, 34°, 38°, 46°, 53°, 59°, and 66°, corresponding to reflection planes (202), (012), (100), (002), (110), (202), (024), (211), and (112), respectively. These sharp peaks suggest a well-defined crystalline structure. Notably, the highest peak at 33° corresponds to the presence of ZnO nanoparticles (ZnO-NPs) [23], which is in agreement with previous research confirming this reflection plane for ZnO-NPs. Additionally, peaks at 23°, 26°, 38°, and 46° confirm the presence of Al_2O_3 nanoparticles (Al_2O_3-NPs) [24]. The crystallite size, calculated using the Debye-Scherrer formula, was found to be 10.658 nm, which is smaller than those reported in earlier studies on Zn-NPs [23], [25] and Al_2O_3-NPs [24]. This decrease in particle size is primarily due to the effects of sonication, which facilitates cavitation, causing a reduction in particle size, increasing surface area, and inducing structural changes [26].

In the case of UV radiation treatment figure 4 (b), the XRD pattern shows peaks at 46°, 26°, 32°, 34°, 38°, 59°, and 65°, corresponding to reflection planes (202), (012), (101), (002), (110), (024), and (214). The highest peak at 32° is similar to the sonication pattern, reflecting the presence of ZnO and Al_2O_3 nanoparticles. However, the crystallite size was measured at 13.566 nm, indicating a larger size than that observed in the sonication-treated nanocomposites. It is observed that the peak is highest peak is higher than the sonication and sonophoto indicates high crystallinity of UV treatments. The increase in crystallite size can be attributed to the UV radiation process, which influences the structural properties of the composite by shifting the crystal size towards larger nanoparticles [20]. Despite the increase in size, this value is still smaller than those reported in previous studies on ZnO and Al_2O_3 nanoparticles. UV treatment plays a key role in modifying the crystal structure by breaking down the polymer matrix and facilitating the formation of smaller, well-dispersed nanoparticles.

The sonophoto treatment Figure 4(a), which combines sonication and UV radiation, produces peaks at 23°, 25°, 34°, 37°, 46°, 52°, 59°, and 65°, corresponding to the reflection planes (202), (012), (100), (002), (110), (202), (024), (211), and (112). The average crystallite size for this method was calculated to be 10.400 nm, which is slightly smaller than the size observed in the UV radiation treatment alone. The reduction in crystallite size is likely due to the synergistic effects of sonication and UV radiation, which work together to promote nanoparticle size reduction and increase uniformity [27]. This combination also shows a shift in the highest peak to 32°, similar to the individual sonication and UV radiation treatments, further confirming the presence of ZnO and Al_2O_3 nanoparticles in the composite.

The XRD results suggest that the crystal structure of the GO-Al-Zn bimetal nanocomposite aligns with a rhombohedral aluminum oxide structure, as indicated by the reference to the JCPDS card no. 10-0173. The integration of graphene oxide (GO) and the Al-Zn bimetal nanoparticles creates a rhombohedral structure due to the stacking of a few layers of flat graphene sheets. This structure results in additional voids between the graphene layers, which further affects the arrangement of the nanoparticles, promoting the formation of a rhombohedral structure. A similar rhombohedral crystal formation was observed in studies involving graphene and Ni-Co bimetal nanoparticles [28]. This type of structure is advantageous as it contributes to the material's stability, mechanical strength, and potential for use in applications such as corrosion-resistant coatings.

The XRD analysis highlights the influence of different synthesis methods—sonication, UV radiation, and sonophoto treatment—on the crystallinity, particle size, and structural properties of the GO-Al-Zn bimetal nanocomposite. Sonication produces smaller particles with increased surface area, while UV radiation shifts the crystal size toward larger nanoparticles. The combined sonophoto treatment optimizes both particle size and crystallinity, resulting in a nanocomposite with promising applications in fields such as corrosion inhibition. The presence of a rhombohedral structure further enhances the material's mechanical and chemical properties, making it a robust candidate for various advanced applications.

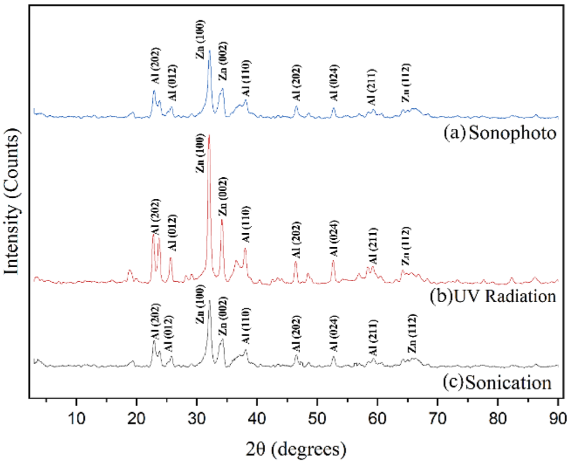

Figure 4: XRD results of GO-Al-Zn bimetal composite by (a) Sonophoto, (b) UV Radiation, and (c) Sonication.

3.1.5 Transmission Electron Microscopy (TEM)

To determine the size and dispersion of nanoparticles in the GO-Al-Zn bimetal nanocomposite synthesized using the sonophoto technique, Transmission Electron Microscopy (TEM) was employed. Figure 5 presents a TEM micrograph and histograms of the nanocomposite, which was prepared using a mixture of graphene oxide (GO) and a bimetallic composition of 55% zinc (Zn) and 45% aluminum (Al). These nanoparticles were synthesized through the synergistic combination of ultrasound and UV radiation, known as the sonophoto technique. The TEM micrograph, taken at 50 nm magnification, shows a wrinkled pattern, indicating the presence of a graphene oxide sheet. The graphene sheet is decorated with irregular dots, which can be identified as Al nanoparticles (Al-NP) and Zn nanoparticles (Zn-NP).

At higher magnification (20 nm), the TEM image provides a clearer view of the structure and dispersion performance of the Zn-Al nanoparticles on the GO sheets. The nanoparticles appear as an interdependent form of crystals with an irregular shape, forming a less porous structure. This structural characteristic suggests a strong interaction between the nanoparticles and the graphene oxide sheet, contributing to the material's stability and dispersion. The irregularity in shape and arrangement of the nanoparticles may be due to the inherent properties of the sonophoto synthesis method, which combines ultrasound to facilitate particle dispersion and UV radiation to assist in size reduction and surface modification of the nanocomposite.

Additionally, the TEM images show the presence of single-layer graphene, which is crucial for achieving the desired dispersion of nanoparticles. At lower magnifications, a more dispersed nanoparticle pattern can be observed, indicating that the sonophoto synthesis method successfully dispersed the nanoparticles across the graphene oxide sheet. This suggests that the combination of sonication and UV radiation is effective in promoting nanoparticle stability and preventing agglomeration, as the particles remain well-distributed on the GO matrix. The stabilization of nanoparticles within the graphene sheet network is critical for ensuring the uniformity and performance of the nanocomposite, especially for applications requiring consistent particle size and dispersion.

Furthermore, the average size of the Al and Zn nanoparticles on the graphene sheet was measured to be 5.59 nm using ImageJ software. The size distribution of more than 97 particles was fitted to a log-normal distribution curve (red line) in the histogram, indicating a nanoparticle size of 5.59 nm with a size distribution of 1.76 nm, which suggests a relatively wide distribution range of nanoparticle sizes. The wide distribution can be attributed to the variability in the synthesis process, where ultrasound and UV radiation can cause fluctuations in particle size and morphology. Interestingly, the nanoparticle size observed in this study is smaller than that of Ag-Au nanoparticles doped in GO composites reported in previous studies [29]. This size reduction highlights the effectiveness of the sonophoto method in producing smaller, more uniformly distributed nanoparticles, which is beneficial for applications where particle size is a critical factor, such as in catalysis, electronic devices, and corrosion resistance.

The TEM analysis confirms that the sonophoto synthesis method produces a well-dispersed mixture of Zn and Al nanoparticles on a single-layer graphene sheet. The method's ability to reduce particle size and enhance dispersion is evident in the small particle size and uniform distribution observed in the TEM micrograph. This highlights the effectiveness of combining ultrasound and UV radiation to synthesize GO-based bimetallic nanocomposites, with potential applications in fields such as nanotechnology and materials science.

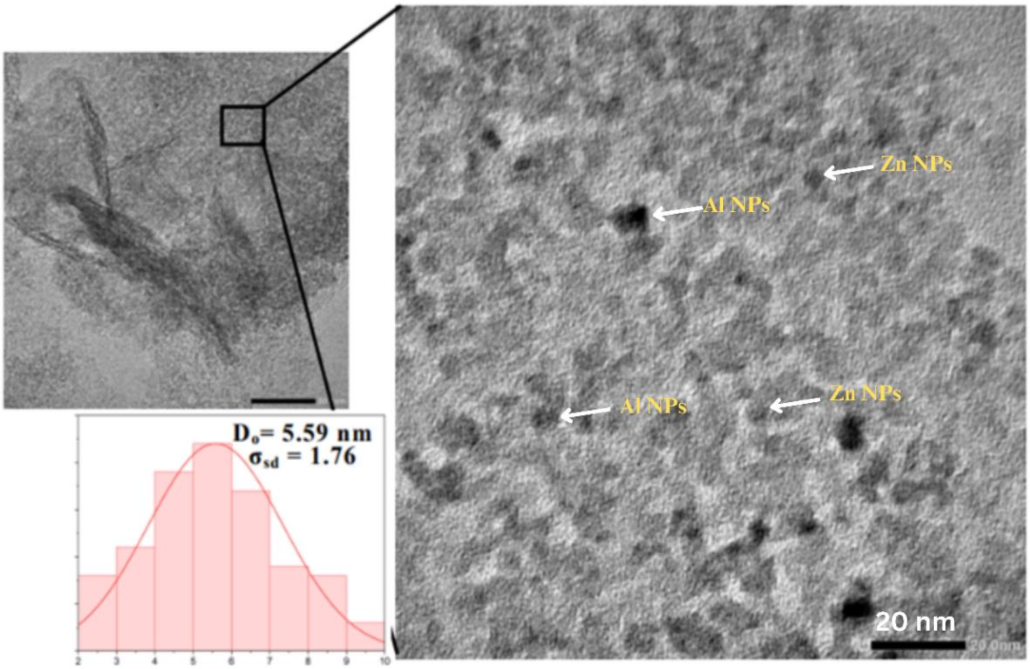

Figure 5: Transmission Electron Microscopy (TEM) of 55% Al-45% Zn GO-Al-Zn bimetal by sonophoto and particle size distribution.

3.2 *Corrosion resistance*

3.2.1 Corrosion rate via weight loss method

The blank samples in Figure 6(a)–(c) exhibited the fastest corrosion rate among the tested samples, indicating the susceptibility of mild steel to corrosion in a saltwater-simulated environment. The linearity of the plots suggests a direct proportionality between corrosion rate and time, highlighting a steady and predictable corrosion process for each treatment method. The highest corrosion rate in the blank sample is expected, as it lacks the protective nanocomposite coating that would inhibit corrosion. This underscores the necessity of an effective anti-corrosive layer in saline environments.

Among the samples, the optimal result was observed in Figure 6(c) with a 1.0 coating composition, which had the lowest corrosion rate. The ratio of nanoparticles dispersed into the polymeric base plays a crucial role in optimizing the coating's corrosion resistance [30]. The spacing between nanoparticles in the coating significantly influences its protective capacity, as it affects how the nanoparticles interact with the corrosive medium. According to Kalajahi *et al.* [31], the efficiency of the nanocomposite depends on both the nanoparticle dispersion and the chemical nature of the nanoparticles themselves. In this study, the 1.0 nanocomposite-to-epoxy resin base ratio was found to be optimal, as it allowed the proper dispersion of nanoparticles, ensuring adequate spacing between them and enhancing the coating’s overall performance.

The sonophoto treatment, which combines sonication and ultraviolet (UV) radiation, was used to synthesize the optimal sample in Figure 6(c). Sonication creates cavitation bubbles that assist in dispersing the nanoparticles more effectively, leading to increased surface area and enhanced performance as a corrosion inhibitor. Additionally, the UV radiation reduces the size distribution of the nanoparticles, further improving their anti-corrosion properties. This synergistic effect of sonophoto treatment aligns with other studies, where nanoparticle size reduction and enhanced mechanical properties resulted in slower corrosion rates [32]. Consequently, the sonophoto-treated sample exhibited the lowest corrosion rate, confirming its efficacy as an optimal anti-corrosion solution for mild steel in saline environments.

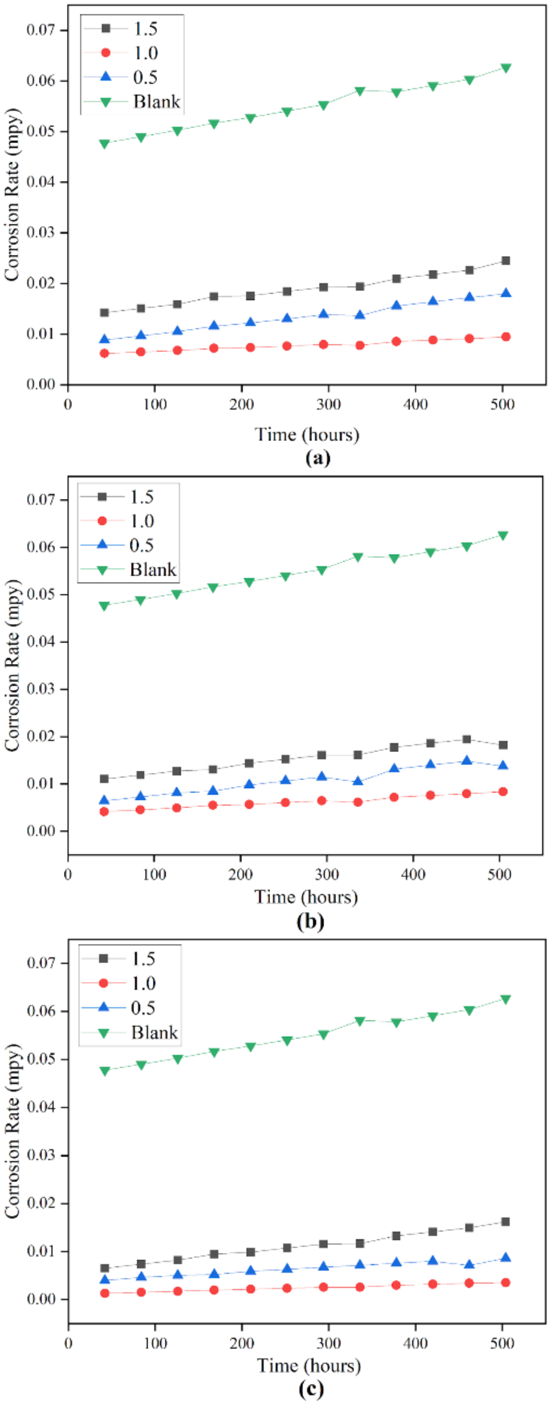

Figure 6: Corrosion rate (mpy) vs time (hours) at varying nanocomposite-to-epoxy resin base coating ratio: 1.5, 1.0, 0.5, and blank at different treatment methods: (a) sonication, (b) ultraviolet radiation, (c) sonophoto.

In contrast, the 1.5 coating composition in Figure 6(a)–(c) consistently demonstrated the highest corrosion rate across all treatment methods, implying that a higher nanoparticle concentration is not necessarily beneficial. The findings suggest that at this ratio, the nanoparticle clustering within the polymeric base becomes excessive, leading to a decrease in performance.

The excessive concentration likely caused aggregation of the nanoparticles, which reduced the coating's effectiveness by disrupting the uniform distribution needed for optimal corrosion protection. Studies suggest that nanoparticle agglomeration in polymeric matrices can hinder the formation of a consistent protective layer, thus increasing susceptibility to corrosion [33]. Therefore, while the synthesis method (sonication, UV, or sonophoto) did not impact the corrosion rate at this higher concentration, the nanoparticle-to-polymer ratio becomes a critical factor for ensuring coating performance [30].

Based on the results, it can be inferred that the nanocomposite-to-epoxy resin ratio must be carefully optimized to avoid particle aggregation and maximize the beneficial effects of both sonication and UV irradiation. The 1.0 ratio allows for a balance between nanoparticle concentration and dispersion, making it the most effective composition for reducing corrosion rates during the 504-hour immersion period. These findings demonstrate the importance of both the synthesis method and nanocomposite ratio in determining the efficacy of corrosion-resistant coatings.

3.2.2 *Inhibition efficiency via weight loss method*

Corrosion inhibition efficiency is largely dependent on the adsorption of organic compounds onto the metal surface, which forms a protective layer and impedes corrosion processes [34]. This is particularly relevant for coatings with dispersed nanoparticles, where the electrochemical properties play a key role in forming this adsorbed layer and, thus, inhibiting corrosion. Figure 7(a)–(c) demonstrates this relationship, where the inhibition efficiency of the synthesized nanoparticles dispersed into the epoxy resin coating decreases over time as the samples are immersed in a saltwater-simulated environment for 504 h. This decreasing trend is expected, as the corrosive environment gradually compromises the coating's protective properties. Notably, the 1.0 coating composition synthesized via both sonication and UV irradiation (sonophoto) shows the slowest decline in inhibition efficiency, as well as the highest initial efficiency, reaching 98.06%. This suggests that the electrochemical properties of this sample were optimized for corrosion inhibition.

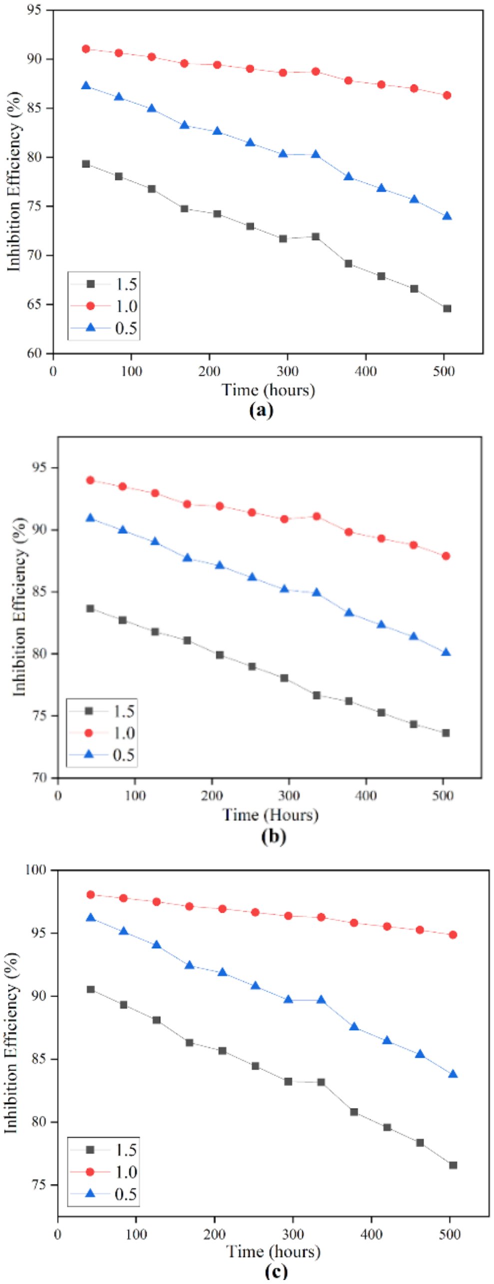

Figure 7: Inhibition efficiency (%) vs time (hours) at varying nanocomposite-to-epoxy resin base coating ratio: 1.5, 1.0, and 0.5 at different treatment methods: (a) sonication, (b) ultraviolet radiation, (c) sonophoto.

The superior performance of the 1.0 nanocomposite-to-epoxy resin ratio can be attributed to its ability to achieve homogeneous dispersion of nanoparticles within the polymeric coating, which is critical for improving its corrosion inhibition properties. The bimetallic zinc and aluminium nanoparticles serve a dual purpose: acting as sacrificial anodes to protect the metal from oxidation and forming a protective barrier that impedes corrosion.

This aligns with previous studies suggesting that proper selection and functionalization of nanoparticles as additives in polymeric coatings can significantly enhance their corrosion protection capabilities. The even distribution of these nanoparticles prevents agglomeration, ensuring that the coating's anti-corrosive properties are maximized [35].

Comparing the results of the 1.5 coating composition in Figure 7(a) and (c), synthesized using sonication and sonophoto methods, respectively, it is clear that both treatments resulted in a similar rate of decrease in inhibition efficiency over time. However, the initial inhibition efficiency was higher for the sonophoto-treated sample, starting at 90.54%, compared to 79.33% for the sonication-only treatment. This indicates that the sonophoto-assisted method is more effective at initially enhancing the electrochemical properties of the bimetallic nanoparticles, leading to better corrosion inhibition. Nevertheless, over time, the degradation rates of both methods are comparable, suggesting that the physical adsorption mechanism of the nanoparticles onto the metal surface is similar for both treatments. This observation implies that while sonophoto synthesis provides higher initial corrosion resistance, the sonication method is still highly effective in ensuring adequate nanoparticle dispersion and improving wear resistance [36].

The sonophoto synthesis method consistently produced higher inhibition efficiencies across all coating compositions, fully utilizing the electrochemical properties of the aluminium-zinc bimetallic nanoparticles. The combination of ultrasonication and ultraviolet light during nanoparticle synthesis not only reduced the corrosion rate of the mild steel but also enhanced the coating's overall inhibition efficiency. This study confirms that optimizing the nanoparticle-to-polymer ratio and synthesis method can significantly impact the corrosion protection offered by such coatings. The synergy between sonication and UV irradiation provides a robust framework for improving the functionality of nanoparticles in corrosion-resistant applications.

3.2.3 Electrochemical property Tafel Plot

Electrochemical corrosion tests of Graphene Oxide (GO) Al-Zn nanocomposites were performed in a 3.5 wt% NaCl solution at room temperature using a Metrohm Autolab PGSTAT128N potentiostat/ galvanostat in a three-electrode setup. The GO Al-Zn nanocomposites, with an exposed area of 1 inch by 1 inch, were used as the working electrode, coated with epoxy, and oriented perpendicular to the pressure direction. Stainless steel served as the counter electrode, while an Ag/AgCl electrode was used as the reference. Potentiodynamic polarization curves were recorded within ±150 mV of the open-circuit potential (OCP) at a scan rate of 1.25 mV/s.

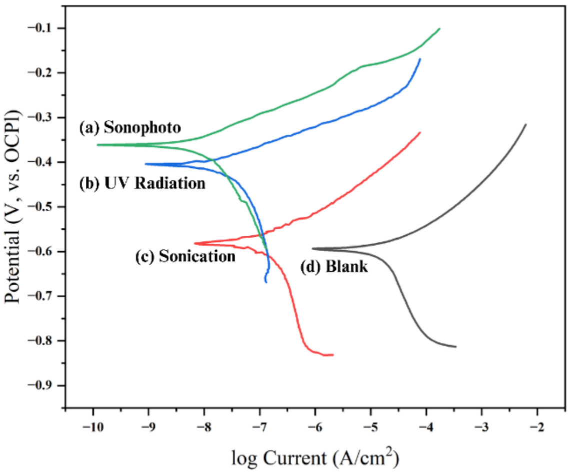

Figure 8: Potentiodynamic polarization curves of (a) sonophoto, (b) uv radiation, (c) sonication, (d) bare MS steel.

Figure 8 illustrates the Tafel polarization curves for the blank mild steel (MS) and the GO Al-Zn-coated MS samples under different treatments. The Tafel curves of the GO Al-Zn-coated samples shift towards more positive potentials compared to the blank MS, with the most significant shift observed in the sample subjected to sonophotocatalysis. This indicates enhanced corrosion resistance for the coated samples. The reduced cathodic and anodic current densities for the GO Al-Zn-coated samples compared to the bare MS suggest that the composite coating effectively mitigates both anodic and cathodic reactions on the substrate surface. The anodic reaction

(Equation (5)) involves zinc (Zn) oxidizing to Zn^{2+} and serving as a sacrificial anode, protecting the underlying steel. The cathodic reaction (Equation (6)) involves the reduction of oxygen in the presence of water, producing hydroxide ions. Aluminium (Equation (7)) contributes by forming a protective oxide layer (Al_2O_3), which acts as a barrier to corrosion [37].

Anodic Reaction: $Zn \rightarrow Zn^{2+} + 2e^{-}$ (5)
Cathodic Reaction: $O_2 + 2H_2O + 4e^{-} \rightarrow 4OH^{-}$ (6)
Aluminum Reaction: $2Al + 3O_2 \rightarrow 2Al_2O_3$ (7)

The electrochemical parameters in Table 2 show that the blank sample had the lowest corrosion potential (E_{corr}) of approximately –598.02 mV and the highest corrosion current density (I_{corr}) of 9709 μA/cm², indicating high susceptibility to corrosion. The GO Al-Zn coatings resulted in improved corrosion resistance, with E_{corr} values of –583.81 mV, –408.32 mV, and –351.29 mV, and reduced I_{corr} values of 876.33 μA/cm², 328.02 μA/cm², and 149.63 μA/cm² for the Sono, UV, and Sonophoto treatments, respectively. These results highlight the significant protective effect of the GO Al-Zn nanocomposite coating. The polarization resistance (Rp) values for the coated samples were substantially higher than those of the blank sample, indicating increased resistance to current flow. Higher Rp values, such as 4.35×10^{8} Ω·cm² for GO Al-Zn/Sono, 5.84×10^{8} Ω·cm² for GO Al-Zn/UV, and 1.38×10^{8} Ω·cm² for GO Al-Zn/Sonophoto, confirm the effectiveness of the coating in providing a passive layer that enhances corrosion resistance [38].

Table 2: Electrochemical corrosion parameters obtained from potentiodynamic polarization curves.

Sample	E_{corr} (mV)	I_{corr} (uA/cm²)	β_a	β_c	R_p (Ω- cm²)	n%	CR (mpy)
Blank	–598.02	0.010247	0.09102	–0.4081	5.24×10^{-6}	-	2.0905×10^{-2}
Sono	–583.81	8.9233×10^{-4}	0.10678	–0.1216	4.35×10^{8}	90.97	1.8869×10^{-3}
UV	–408.32	3.60335×10^{-4}	0.046	0.0514	5.84×10^{8}	96.62	7.0667×10^{-4}
Sonophoto	–351.29	1.3057×10^{-4}	0.01745	–0.0274	1.38×10^{8}	98.45	3.2218×10^{-4}

Table 3: Functional groups of Fourier Transform Infrared (FTIR) spectroscopy for coated mild steel.

Wavenumber (cm⁻¹)	Functional Group	Sonophoto		UV Radiation		Sonication	
		A*	B*	A*	B*	A*	B*
		Intensity	Intensity	Intensity	Intensity	Intensity	Intensity
2928	C-H bend	Weak	Weak	Weak	Weak	Weak	Weak
1608	C=C stretch	Weak	Weak	Weak	Medium	Weak	Weak
1508	C-O-C (epoxide)	Medium	Medium	Medium	Medium	Medium	Weak
1457	C=C stretch	Weak	Weak	Weak	Weak	Weak	Weak
1362	C-O-C stretch	Weak	Weak	Weak	Weak	Weak	Weak
1295	C-O-C stretch	Weak	Weak	Weak	Weak	Weak	Weak
1244	C-O-C stretch	Medium	Medium	Medium	Medium	Medium	Medium
1181	C-N scissor	Medium	Medium	Medium	Medium	Medium	Medium
1035	C-N bend	Medium	Medium	Medium	Medium	Medium	Medium
827	Al-O scissor	Medium	Medium	Medium	Strong	Strong	Medium
736	Al-O	Weak	Weak	Weak	Weak	Weak	Weak
698	Zn-O	Weak	Weak	Weak	Weak	Weak	Weak

Note: A* - GO-Al-Zn Coating before submersion; B* - GO-Al-Zn Coating after submersion

The incorporation of graphene oxide into the Al-Zn bimetal nanocomposite further improves corrosion resistance through both physical and chemical mechanisms. Graphene oxide enhances cathodic protection by forming a dense protective layer of corrosion products on the coating's surface. Traditional Zn/Al coatings provide cathodic protection through sacrificial corrosion, creating a “labyrinth effect” that impedes the penetration of corrosive agents. Graphene's lamellar structure fills defects in the coating, reduces porosity, and inhibits corrosive species diffusion. This barrier effect increases the diffusion path length for aggressive ions, strengthening the protective nature of the corrosion product layer [39], [40].

Among the treatments, sonophotocatalysis showed the best performance, with a corrosion rate of 3.2218×10^{-4} mpy and a corrosion inhibition efficiency of 98.45%. Moreover, the higher potential denotes that the material is more noble or less reactive and the lower current indicates that the rate of corrosion is slower. This demonstrates the synergistic effect of sonication and UV treatments in achieving superior corrosion resistance. The sonication treatment alone achieved a corrosion rate of 1.8869×10^{-3} mpy, while UV treatment resulted in a rate of 7.0667×10^{-4} mpy. These findings suggest that combining both treatments enhances the coating's protective properties more effectively than either method alone.

3.3 *Characterization of epoxy GO-Al-Zn bimetal nanocomposite coating*

3.3.1 Fourier Transform Infrared Spectroscopy (FTIR) of GO-Al-Zn composite coating

Figure 9 illustrates the FTIR analysis of the coated mild steel coupons before and after submersion in a 3.5 wt% NaCl solution, simulating seawater, for 21 days (504 h) without direct sunlight exposure. Table 3 summarizes the functional groups identified in these coatings, with the FTIR spectra showing transmittance versus wavelength curves and mid-IR spectra.

The FTIR spectrum revealed that peaks in the single bond region (2500–4000 cm^{-1}) appear only at 2928 cm^{-1}, indicating the presence of C-H bonds. The triple bond region (2000–2500 cm^{-1}) lacks detectable peaks, likely due to the low polarity of alkyne groups, which are less detectable with FTIR. In the double bond region (1500–2000 cm^{-1}), a prominent peak at 1508 cm^{-1} corresponds to C-O-C (epoxide), while peaks at 1608 cm^{-1} and 1457 cm^{-1} suggest C=C stretching vibrations. In the fingerprint region (500–1500 cm^{-1}), multiple peaks are detected: at 1362, 1295, and 1244 cm^{-1}, associated with cyclic ether (C-O-C) stretching [19], [40]. Peaks at 1181 and 1035 cm^{-1} correspond to the C-N group [15], while 698 cm^{-1} confirms Zn-O [14], and 827 and 736 cm^{-1} verify Al-O [41].

The data indicate that while there are slight differences in peak intensities, the positions of the peaks remain relatively consistent before and after submersion, suggesting the preservation of functional groups. Notably, increased peak intensity in the sonophotocatalysis and UV radiation-treated samples before and after submersion indicates enhanced stability or formation of these functional groups, likely improving the coating's protective properties.

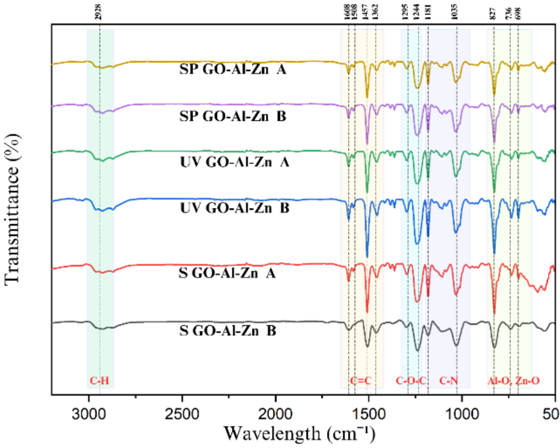

Figure 9: FTIR Analysis of coated mild steel coupons before and after salt simulation.

Conversely, the sonication-only treatment shows a reduction in peak intensity, which may suggest that sonication alone does not effectively maintain or enhance the functional groups responsible for corrosion protection. This reduction could result from the disruption or alteration of these groups under ultrasonic conditions.

The presence of key oxygen-containing functional groups, such as cyclic ethers (C-O-C), Zn-O, and Al-O, underscores the GO-Al-Zn bimetal nanocomposite coating's anti-corrosion effectiveness [42]. These groups form stable, protective layers that inhibit corrosive reactions on the mild steel surface [43]. The FTIR results suggest that sonication and UV radiation treatments enhance the protective properties of the coating compared to sonication alone.

The FTIR analysis confirms the presence and stability of functional groups contributing to the corrosion resistance of the GO-Al-Zn nanocomposite coating. The results highlight the effectiveness of sonication and UV treatments in enhancing the coating's protective qualities, while sonication alone may be less effective. Future studies should explore the reasons behind these observations and optimize treatment methods to further improve coating stability and performance.

3.3.2 SEM of GO-Bimetals nanoparticles coating

Figure 10(a) and (b) display the morphology of GO-Bimetal nanocomposites synthesized under ultrasonic conditions as observed through scanning electron microscopy (SEM). Before submersion in the 3.5 wt% salt solution, sono-coating Figure 10(a) revealed nanoparticles with irregular sizes and sparse structures, suggesting that the ultrasonic method yields a non-uniform dispersion of nanoparticles. This initial morphology indicates that while the ultrasonic process can disperse nanoparticles, it may not achieve a stable or consistent distribution.

After submersion in the salt solution, sono-coating (b) shows a significant increase in amorphous structures and a pronounced tendency for nanoparticles to agglomerate. This change is indicative of enhanced particle interactions facilitated by the ionic environment of the salt solution, which likely increases the attractive forces between nanoparticles and promotes their aggregation. Such agglomeration can diminish the effectiveness of the coating by reducing its uniformity and potentially compromising its protective properties [10].

Figure 10(c) and (d) In the case of UV-coating A Figure 10(c), prior to immersion in a salt solution, the SEM images showed the formation of a stable surface layer, which contributed to a smooth surface morphology. This smoothness suggests proper dispersion of nanoparticles and efficient bonding facilitated by the UV-coating process, resulting in fewer surface irregularities and better protective properties. In contrast, upon immersion, UV-coating B Figure 10(d) exhibited agglomerated, irregularly shaped NPs, leading to a significantly rougher surface. The roughness and aggregation observed were likely caused by the interaction of the nanoparticles with the salt solution, which promoted the clustering of particles. This aggregation can compromise the coating's effectiveness by creating more sites for corrosion initiation and reducing uniformity. The salt solution introduces ionic species that reduce the repulsive forces between particles, leading to poor dispersion and larger agglomerates, which ultimately affects the coating's stability and performance. While the UV-assisted coating method can create stable and smooth surfaces in less aggressive environments, the observed surface roughness and aggregation in salt-exposed coating B suggest a need for improved stabilization techniques to maintain nanoparticle dispersion in corrosive conditions [28].

Figure 10(e) and (f) illustrate the SEM analysis of GO-Bimetal nanocomposites synthesized using sonophoto-assisted coating. Before submersion, sonophoto-coating Figure 10(e) displays a more organized and spacious nanoparticle arrangement with relatively disordered structures. This suggests that the sonophoto-assisted method achieves a better initial dispersion compared to the ultrasonic method. However, after submersion, sonophoto-coating Figure 10(f) shows substantial agglomeration and a rougher surface. The increased agglomeration in this case may result from interactions between nanoparticles and the salt solution, which induce clustering and roughen the surface.

The SEM results underscore the influence of synthesis methods on nanoparticle morphology and stability. While the ultrasonic method initially disperses nanoparticles irregularly, it shows a marked increase in agglomeration upon exposure to a salt solution, reflecting instability in corrosive environments. Conversely, the sonophoto-assisted method provides a more uniform nanoparticle distribution initially but also leads to significant agglomeration post-submersion. These findings suggest that both methods result in coatings susceptible to particle aggregation in saline conditions, which may affect their performance in real-world applications.

The SEM analysis highlights that both ultrasonic and sonophoto-assisted synthesis methods lead to increased nanoparticle agglomeration after exposure to a salt solution. The initial particle distribution achieved by these methods varies, with sonophoto-assisted coating showing a more stable arrangement before submersion. However, both methods exhibit similar issues with agglomeration under corrosive conditions. These results indicate the need for further optimization of synthesis techniques to enhance the stability and performance of GO-Bimetal nanocomposite coatings in aggressive environments. Future research should focus on strategies to mitigate agglomeration and improve the durability of these coatings.

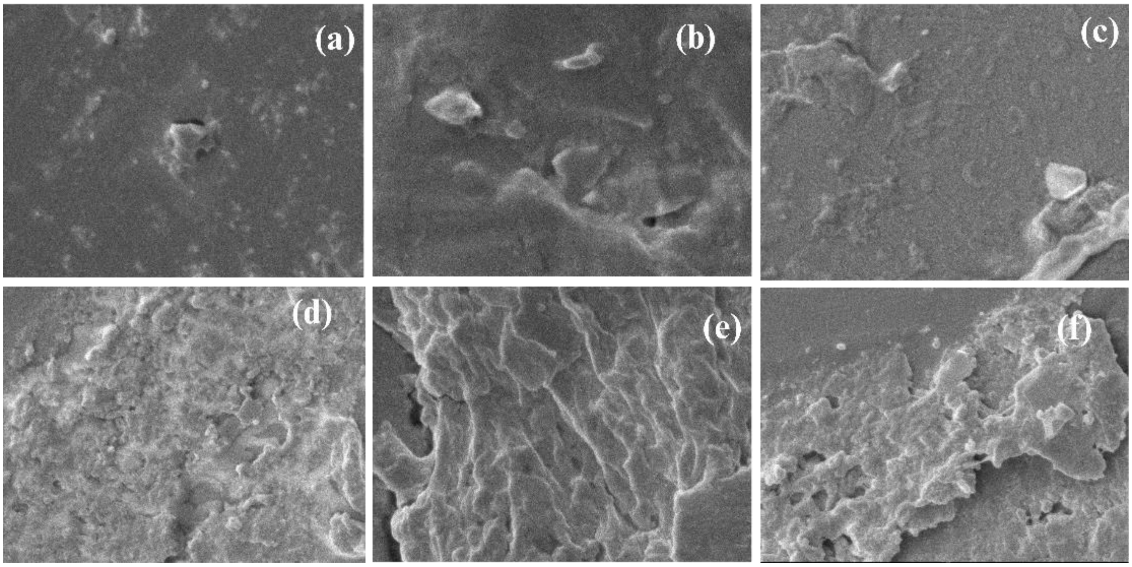

Figure 10: SEM of GO-Bimetals nanoparticles coating by sonication (a) before and (b) after, UV radiation (c) before and (d) after submerging to salt solution, and sonophoto (e) before and (f) after submerging to salt solution.

4 Conclusions

This research investigated a novel bimetallic nanocomposite (GO-Al-Zn) for its potential in corrosion protection. The study successfully synthesized the nanocomposite and identified key factors for optimal performance. A 55% aluminium and 45% zinc composition synthesized using the sonophoto method for 15 min yielded the highest production and best results. Different synthesis methods influenced the morphology and size of the nanoparticles, with the sonophoto method offering the most desirable outcome due to its ability to achieve both good particle dispersion and reduced size, leading to a larger surface area. The analysis confirmed the successful synthesis of the GO-Al-Zn with the intended composition and structure. All treatment methods significantly improved corrosion resistance, with the sonophoto method achieving the highest inhibition efficiency at 98% due to its synergistic effect. This combined approach also increased the coating's inhibition efficiency by 10% compared to using sonication or UV radiation alone. Finally, the study highlights the GO - 55% Al - 45% Zn nanocomposite prepared via the sonophoto method with a 1% epoxy coating composition as particularly promising for real-world applications in corrosion prevention.

This study was limited to fixed time exposures, a constant temperature, and a specific corrosion medium (3.5 wt% NaCl solution). These controlled conditions may not fully reflect real-world scenarios where variable environmental factors exist.

Future studies should investigate the influence of varying temperatures to assess how changes in temperature affect corrosion kinetics and nanocomposite stability. Extending the exposure time would also help understand the degradation behavior of the synthesized nanoparticles over longer periods. A major challenge lies in developing an experimental setup that simulates diverse environmental conditions. Creating such a system would allow researchers to evaluate corrosion rates in specific regions around the world, making the findings more applicable to real-world scenarios.

This research demonstrates the potential of the GO-Al-Zn nanocomposite as a promising corrosion inhibitor. The sonophoto method offers a promising approach for synthesizing this material with optimal properties. However, further research is needed to address the limitations and explore the nanocomposite’s performance in real-world conditions.

Acknowledgments

This study was supported by the Center of Research and Development (CRD) and the Chemical Engineering Department of Adamson University.

Author Contributions

C.E.: drafting and conceptualization, introduction, methodology, interpretation, experiment, data custodian, data interpreter, reviewing and editing; M.A.: introduction, methodology, interpretation, experiment, editing; H.C.: introduction, interpretation, experiment, reviewing and editing; D.A.F.: introduction, methodology, interpretation, experiment, reviewing and editing; K.P.: introduction, methodology, interpretation, experiment, reviewing and editing; A.E.: conceptualization, reviewing; R.V.R: drafting and conceptualization, reviewing and editing, project administration. All Authors have agreed to published version of manuscript.

Conflicts of Interest

The authors declare that there is no conflict of interest regarding the publication of this article.

References

[1] B. Dong, W. Liu, T. Zhang, L. Chen, Y. Fan, Y. Zhao, W. Yang, and W. Banthukul, "Corrosion failure analysis of low alloy steel and mild steel rebar in tropical marine atmospheric environment: Outdoor exposure and indoor test," *Engineering Failure Analysis*, vol. 129, Mar. 2021, Art. no. 105720, doi: 10.1016/j.engfailanal.2021.105720.

[2] Y. Liu, M. Liu, X. Lu, and Z. Wang, "Effect of temperature and ultraviolet radiation on corrosion behavior of mild steel in high humidity tropical marine atmosphere," *Materials Chemistry and Physics*, 2021, Art. no. 124962, doi: 10.1016/j.matchemphys.2021.124962.

[3] M. Faccini, L. Bautista, L. Soldi, A. M. Escobar, M. Altavilla, M. Calvet, A. Domènech, and E. Domínguez, "Environmentally friendly anticorrosive polymeric coatings," *Applied Sciences (Switzerland)*, vol. 11, no. 8, 2021, doi: 10.3390/app11083446.

[4] O. Dagdag, R. Hsissou, A. E. Harfi, A. Berisha, Z. Safi, C. Verma, E. E. Ebenso, M. Ebn Touhami, and M. E. Gouri, "Fabrication of polymer based epoxy resin as effective anti-corrosive coating for steel: Computational modeling reinforced experimental studies," *Surfaces and Interfaces*, vol. 18, 2020, doi: 10.1016/j.surfin.2020.100454.

[5] A. S. Ganie, S. Bano, N. Khan, S. Sultana, Z. Rehman, M. M. Rahman, S. Sabir, F. Coulon, and M. Z. Khan, "Nanoremediation technologies for sustainable remediation of contaminated environments: Recent advances and challenges," *Chemosphere*, vol. 275, 2021, Art. no. 130065, doi: 10.1016/j.chemosphere.2021.130065.

[6] S. Yadav, A. P. S. Raman, M. B. Singh, I. Massey, P. Singh, C. Verma, and A. AlFantazi, "Green nanoparticles for advanced corrosion protection: Current perspectives and future prospects," *Applied Surface Science Advances*, vol. 21, Jun. 2024, Art. no. 100605, doi: 10.1016/j.apsadv.2024.100605.

[7] S. Liu, Y. Zhu, X. Zheng, X. Lai, R. Jia, and X. Yuan, "Graphene oxide modified by zirconium dioxide to enhance the corrosion resistance of Zinc/Aluminum coatings," *Diamond and Related Materials*, vol. 108, Apr. 2020, Art. no. 107868, doi: 10.1016/j.diamond.2020.107868.

[8] K. A. Chang, S. L. Ley, M. Y. Lee, H. Y. Yaw, S. W. Lee, L. Y. Chew, Y. P. Neo, and K. W. Kong, "Determination of nutritional constituents, antioxidant properties, and α-amylase inhibitory activity of *Sechium edule* (chayote) shoot from different extraction solvents and cooking methods," *LWT*, vol. 151, Nov. 2021, Art. no. 112177, doi: 10.1016/j.lwt.2021.112177.

[9] R. Mohammadkhani, M. Ramezanzadeh, S. Akbarzadeh, G. Bahlakeh, and B. Ramezanzadeh, "Graphene oxide nanoplatforms reduction by green plant-sourced organic compounds for construction of an active anti-corrosion coating; experimental/electronic-scale DFT-D modeling studies," *Chemical Engineering Journal*, vol. 397, Oct. 2020, Art. no. 125433, doi: 10.1016/j.cej.2020.125433.

[10] A. Singh, K. R. Ansari, D. S. Chauhan, M. A. Quraishi, H. Lgaz, and I.-M. Chung, "Comprehensive investigation of steel corrosion inhibition at macro/micro level by ecofriendly green corrosion inhibitor in 15% HCl medium," *Journal of Colloid and Interface Science*, vol. 560, pp. 225–236, Feb. 2020, doi: 10.1016/j.jcis.2019.10.040.

[11] P. R. Sivakumar and A. P. Srikanth, "Green corrosion inhibitor: A comparative study," Sādhanā, vol. 45, no. 1, Feb. 2020, doi: 10.1007/s12046-020-1283-x.

[12] N. Baig, I. Kammakakam, and W. Falath, "Nanomaterials: A review of synthesis methods, properties, recent progress, and challenges,"

Materials Advances, vol. 2, no. 6, pp. 1821–1871, Feb. 2021, doi: 10.1039/d0ma00807a.

[13] A. K. Saleh, A. S. Shaban, M. A. Diab, D. Debarnot, and A. S. Elzaref, "Green synthesis and characterization of aluminum oxide nanoparticles using *Phoenix dactylifera* seed extract along with antimicrobial activity, phytotoxicity, and cytological effects on *Vicia faba* seeds," *Biomass Conversion and Biorefinery*, Sep. 2023, doi: 10.1007/s13399-023-04800-x.

[14] S. Bashir, M. S. Awan, M. A. Farrukh, R. Naidu, S. A. Khan, N. Rafique, S. Ali, I. Hayat, I. Hussain, and M. Z. Khan, "In vivo (*Albino mice*) and in vitro assimilation and toxicity of zinc oxide nanoparticles in food materials," *International Journal of Nanomedicine*, vol. 17, pp. 4073–4085, Sep. 2022, doi: 10.2147/ijn.s372343.

[15] A. S. Daulay, Ridwanto, R. A. Syahputra, and A. Nafitri, "Antioxidant activity test of Chayote (*Sechium edule* (Jacq.) Swartz) ethanol extract using DPPH method," *Journal of Physics: Conference Series*, vol. 1819, no. 1, Mar. 2021, Art. no. 012035, doi: 10.1088/1742-6596/1819/1/012035.

[16] A. C. Vilando, V. DC, and F. Joie, *Utilization of Low-Cost Waste Materials in Wastewater Treatments*. Amsterdam, Netherlands: Elsevier, pp. 99–119, Jan. 2021, doi: 10.1016/b978-0-12-823031-2.00018-5.

[17] F. Rolle and M. Sega, "Use of FTIR spectroscopy for the measurement of CO_2 carbon stable isotope ratios," in *19th International Congress of Metrology*, Sep. 2019, doi: 10.1051/metrology/201905002.

[18] X. Wei, X. Bao, L. Yu, H. Liu, K. Lu, L. Chen, and W. Li, "Correlation between gel strength of starch-based hydrogel and slow release behavior of its embedded urea," *Journal of Polymers and the Environment*, vol. 28, no. 3, pp. 863–870, Jan. 2020, doi: 10.1007/s10924-020-01653-7.

[19] Y. Y. Lim, A. Miskon, A. M. A. Zaidi, M. M. H. M. Ahmad, and M. Abu Bakar, "Structural characterization analyses of low brass filler biomaterial for hard tissue implanted scaffold applications," *Materials*, vol. 15, no. 4, p. 1421, Feb. 2022, doi: 10.3390/ma15041421.

[20] K. Paperzh, A. Alekseenko, O. Safronenko, A. Nikulin, I. Pankov, and V. Guterman, "UV radiation effect on the microstructure and performance of electrocatalysts based on small Pt nanoparticles synthesized in the liquid phase," *Colloid and Interface Science Communications*, vol. 45, Nov. 2021, Art. no. 100517, doi: 10.1016/j.colcom.2021.100517.

[21] D. G. Jr. Goodwin, S.-J. Shen, Y. Lyu, R. Lankone, A. C. Barrios, S. Kabir, F. Perreault, W. Wohlleben, T. Nguyen, and L. Sung, "Graphene/polymer nanocomposite degradation by ultraviolet light: The effects of graphene nanofillers and their potential for release," *Polymer Degradation and Stability*, vol. 182, Dec. 2020, Art. no. 109365, doi: 10.1016/j.polymdegradstab.2020.109365.

[22] L. Gao, S. Mei, H. Ma, and X. Chen, "Ultrasound-assisted green synthesis of gold nanoparticles using citrus peel extract and their enhanced anti-inflammatory activity," *Ultrasonics Sonochemistry*, vol. 83, Feb. 2022, Art. no. 105940, doi: 10.1016/j.ultsonch.2022.105940.

[23] S. Faisal, H. Jan, S.A. Shah, S. Shah, A. Khan, M. T. Akbar, M. Rizwan, F. Jan, Wajidullah, N. Akhtar, A. Khattak, and S. Syed, "Green synthesis of zinc oxide (ZnO) nanoparticles using aqueous fruit extracts of myristica fragrans: Their characterizations and biological and environmental applications," *ACS Omega*, vol. 6, no. 14, pp. 9709–9722, Mar. 2021, doi: 10.1021/acsomega.1c00310.

[24] M. N. Nduni, A. M. Osano, and B. Chaka, "Synthesis and characterization of aluminium oxide nanoparticles from waste aluminium foil and potential application in aluminium-ion cell," *Cleaner Engineering and Technology*, vol. 3, Jul. 2021, Art. no. 100108, doi: 10.1016/j.clet.2021.100108.

[25] S. Das, S. Pramanik, M. Hossain, S. Mukherjee, C. Rajak, P. Pal, and P. K. Kuiri, "Correlation of defects and crystallite size of ZnO nanoparticles synthesized by mechanical milling," *Indian Journal of Physics*, vol. 97, no. 14, pp. 4263–4276, May 2023, doi: 10.1007/s12648-023-02763-3.

[26] D. Y. Hoo, Z. L. Low, D. Y. S. Low, S. Y. Tang, S. Manickam, K. W. Tan, and Z. H. Ban, "Ultrasonic cavitation: An effective cleaner and greener intensification technology in the extraction and surface modification of nanocellulose," *Ultrasonics Sonochemistry*, vol. 90, Nov. 2022, Art. no. 106176, doi: 10.1016/j.ultsonch.2022.106176

[27] A. Aliyu and C. Srivastava, “Correlation between growth texture, crystallite size, lattice strain and corrosion behavior of copper-carbon nanotube composite coatings,” *Surface and Coatings Technology*, vol. 405, Nov. 2020, Art. no. 126596, doi: 10.1016/j.surfcoat.2020.126596.

[28] S. Ying, Z. Guan, P. C. Ofoegbu, P. Clubb, C. Rico, F. He, and J. Hong, “Green synthesis of nanoparticles: Current developments and limitations,” *Environmental Technology & Innovation*, vol. 26, May 2022, Art. no. 102336, doi: 10.1016/j.eti.2022.102336.

[29] B. Zhu, T. Wan, J. Li, C. Meng, X. Du, G. Liu, and Y. Guan, “Graphene-wrapped bimetallic nanoparticles bifunctional electrocatalyst for rechargeable Zn-air battery,” *Journal of Electroanalytical Chemistry*, vol. 927, Nov. 2022, Art. no. 116946, doi: 10.1016/j.jelechem. 2022.116946.

[30] Y. Y. Lim, A. Miskon, and A. M. A. Zaidi, “Structural strength analyses for low brass filler biomaterial with anti-trauma effects in articular cartilage scaffold design,” *Materials*, vol. 15, no. 13, Jun. 2022, Art. no. 4446, doi: 10.3390/ma 15134446.

[31] S. T. Kalajahi, A. Misra, and A. Koerdt, “Nanotechnology to mitigate microbiologically influenced corrosion (MIC),” *Frontiers in Nanotechnology*, vol. 6, Apr. 2024, doi: 10.3389/ fnano.2024.1340352.

[32] J. Bao, S. Guo, D. Fan, J. Cheng, Y. Zhang, and X. Pang, “Sonoactivated Nanomaterials: A potent armament for wastewater treatment,” Ultrasonics Sonochemistry, vol. 99, Oct. 2023, Art. no. 106569, doi: 10.1016/j.ultsonch.2023. 106569.

[33] Y. Sui, Y. Cui, X. Meng, and Q. Zhou, “Research progress on the correlation between properties of nanoparticles and their dispersion states in polymer matrix,” *Journal of Applied Polymer Science*, vol. 139, no. 19, Dec. 2021, Art. no. 52096, doi: 10.1002/app.52096.

[34] T. Attar, A. Benchadli, and E. Choukchou-Braham, “Inhibition of corrosion of copper by polyvinylpyrrolidone-iodine in sulfuric acid medium,” *Algerian Journal of Materials Chemistry*, vol. 05, pp. 01–08, Jan. 2022, doi: 10.5281/zenodo.5855835.

[35] A. B. Rashid, M. Haque, S. M. M. Islam, and K. M. R. U. Labib, “Nanotechnology-enhanced fiber-reinforced polymer composites: Recent advancements on processing techniques and applications,” *Heliyon*, vol. 10, no. 2, Jan. 2024, Art. no. e24692, doi: 10.1016/j.heliyon.2024.e24692.

[36] K. A. Altammar, “A review on nanoparticles: Characteristics, synthesis, applications, and challenges,” *Frontiers in Microbiology*, vol. 14, Apr. 2023, Art. no. 1155622, doi: 10.3389/ fmicb.2023.1155622.

[37] L. Xiao, Q. Liu, J. Wang, N. Chen, J. Chen, J. Song, X. Zhang, and K. Xiao, “Study on corrosion mechanism of Al–Zn coatings in the simulated polluted marine atmosphere,” *Journal of Materials Research and Technology*, vol. 25, pp. 6446–6458, Jul. 2023, doi: 10.1016/j.jmrt. 2023.07.091.

[38] B. Shyamvarnan, S. Shanmugapriya, J. Arockia Selvi, P. Kamaraj, and R. Mohankumar, “Corrosion inhibition effect of Elettaria cardamomum extract on mild steel in 3.5% NaCl medium,” *Materials Today: Proceedings*, vol. 40, pp. S192–S197, 2021, doi: 10.1016/j.matpr. 2020.09.085.

[39] Q. Shi, H. Wu, P. Zhang, D. Wang, J. Wang, and X. Jie, “Balanced anti-corrosion action of reduced graphene oxide in Zn-Al coating during medium-term exposure to NaCl solution,” *Coatings*, vol. 13, no. 9, p. 1570, Sep. 2023, doi: 10.3390/coatings13091570.

[40] A. B. D. Nandiyanto, R. Ragadhita, and M. Fiandini, “Interpretation of fourier transform infrared spectra (FTIR): A practical approach in the polymer/plastic thermal decomposition,” *Indonesian Journal of Science and Technology*, vol. 8, no. 1, pp. 113–126, Sep. 2022, doi: 10.17509/ijost.v8i1.53297.

[41] E. Bibi, “Synthesis and characterization of Al_2O_3 nanoparticles from Trachyspermum ammi,” *Agronomy & Agricultural Science*, vol. 6, no. 2, pp. 1–5, Dec. 2023, doi: 10.24966/aas-8292/ 100050.

[42] O. R. Kam, I. Garikoe, C. Bakouan, and B. Guel, “Low-cost synthesis of alumina nanoparticles and their usage for bisphenol-A removal from aqueous solutions,” *Processes*, vol. 9, no. 10, p. 1709, Sep. 2021, doi: 10.3390/pr9101709.

[43] A. A. Al-Amiery, W. N. R. W. Isahak, and W. K. Al-Azzawi, “Corrosion inhibitors: Natural and synthetic organic inhibitors,” *Lubricants*, vol. 11, no. 4, p. 174, Apr. 2023, doi: 10.3390/ lubricants11040174.